First-principles study of size- and edge-dependent properties of MXene nanoribbons

Liang Hong, Robert F. Klie, and Serdar Öğüt
Department of Physics, University of Illinois at Chicago, Chicago, Illinois 60607, USA
(Received 14 October 2015; published 9 March 2016)

We present results and analyses from first-principles calculations aimed at exploring the size- and edge-dependent properties of a wide range of MXene nanoribbons cut from two-dimensional (2D) semiconducting MXenes. The nanoribbons are classified by their edge types (armchair versus zigzag), the composition and sequencing of the terminating atomic lines, and the lowest-energy structural models of their 2D counterparts. The semiconducting versus metallic nature of the nanoribbons is well explained using an electron counting rule for the edge dangling bonds. For semiconducting nanoribbons, the band-gap evolution as a function of ribbon size is shown to be dependent on the lowest-energy structural model, and determined by a combination of factors such as quantum confinement, the energetic location of the edge states, and the strength of the *d*-*d* hybridization. Nanoribbons cut from 2D MXenes with asymmetric surfaces are found to have bent ground-state structures with curvatures increasing as the size of the ribbon decreases.

DOI: 10.1103/PhysRevB.93.115412

I. INTRODUCTION

Two-dimensional (2D) materials have been of significant interest owing to their unique properties and potential technological applications in nanoscale devices. By confinement of 2D materials, one-dimensional (1D) nanostructures, such as nanoribbons and nanotubes, can be created with considerably different physical properties from their 2D counterparts due to quantum confinement and surface effects [1–3]. For example, the widely studied 2D graphene is a semimetal, whereas the 1D graphene nanoribbons can be semiconductors with band gaps that can be tuned as a function of the ribbon width and edge configuration (armchair versus zigzag) [2–11]. Studies on similar honeycomb-shaped nanoribbons obtained from 2D silicene [12–15], boron nitride [16–18], transition-metal dichalcogenides (TMDs) [19–23], have also revealed interesting size- and edge-dependent properties in these 1D nanostructures. Some of the nanoribbons mentioned above have been fabricated using methods such as lithography, bottom-up synthesis, and unzipping nanotubes [24–26].

Recently, another class of novel 2D materials, known as MXenes, has drawn significant attention stemming from their excellent properties such as high damage tolerance, oxidation resistance, and electrical and thermal conductivity [27–34], and might be functionalized for other novel physical and chemical applications. Experimentally, MXenes have been synthesized by exfoliation from the bulk MAX phases [31–34]. The MAX phases are a large family of layered, hexagonal carbides and nitrides with the general formula $M_{n+1}AX_n$, where $n = 1$–3, M is an early transition metal, A is an A-group (mostly IIIA and IVA) element, and X is either carbon and/or nitrogen [35–38]. MXenes can be achieved by etching the A layers in MAX solids using hydrofluoric acid solution. As a result, the surfaces of MXenes are always chemically functionalized/terminated with selective groups, such as O, F, or OH [32,33]. Accordingly, bare MXenes have the formula $M_{n+1}X_n$ while functionalized MXenes have the formula $M_{n+1}X_nT_2$, where T represents functional terminations.

In the last few years, the mechanical and electronic properties of 2D MXenes have been intensively studied using first-principles calculations [39–53]. A previous study has shown that the thinnest and thicker MXenes exhibit different electronic properties since the density of states (DOS) at the Fermi level of thicker MXenes is much higher than that for the thinnest MXenes [40]. All of the bare MXenes are found to be metallic; however, after functionalization, some of the thinnest MXenes, such as Ti_2CO_2, Zr_2CO_2, Hf_2CO_2, Sc_2CO_2, Sc_2CF_2, and $Sc_2C(OH)_2$, become semiconducting with band gaps ranging from 0.24 to 1.8 eV [39]. So far, only two first-principles studies have been reported on selected MXene nanoribbons: Zhao *et al.* examined the structural and electronic properties of bare and O-functionalized Ti_2C, Ti_3C_2, and V_2C nanoribbons at a few selected sizes [48], and Zhang *et al.* focused on the carrier mobility of Ti_2CO_2 nanoribbons [54].

In this work, we present results and analyses of our first-principles calculations on a wide range of functionalized MXene nanoribbons. Our focus is on nanoribbons derived from 2D monolayers of the form M_2XT_2 with M = Sc, Y, La, Ti, Zr, Hf, X = C, and T = O, F, OH. Of these 18 possibilities, 12 of them are found to have band gaps at the Fermi level, and we focus on the structural and electronic properties of nanoribbons obtained from these semiconducting MXene monolayers. We perform a systematic investigation of size- and edge-dependent properties by classifying all possible armchair and zigzag edge terminations. Our results show that the semiconducting versus metallic character of MXene nanoribbons is largely dependent on their edge types, and can be understood in terms of an electron counting rule. For the semiconducting nanoribbons, the band-gap evolution as a function of ribbon size is, in general, dependent on the lowest-energy structural models of their 2D counterparts, and determined by a combination of factors such as quantum confinement, the energetic location of edge states, and the strength of the *d*-*d* hybridization imposed by geometrical factors. The rest of the paper is organized as follows. In Sec. II, we briefly discuss the technical details of our first-principles calculations, present the three structural models for 2D functionalized MXenes, and classify all possible armchair and zigzag nanoribbons that can be obtained from these models. In Sec. III, we first examine the structural and electronic properties of semiconducting 2D MXenes. Next, we consider and present results on three types of MXene nanoribbons: (1) Ti_2CO_2, (2) Sc_2CO_2, and (3) Sc_2CF_2 and

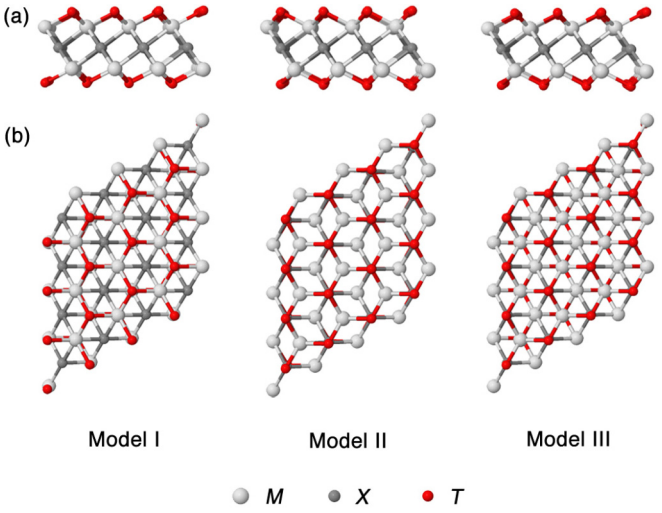

FIG. 1. (a) Side views and (b) top views of three models of the functionalized M_2X systems (i.e., M_2XT_2) in $4 \times 4 \times 1$ unit cell. M, X, and T elements are represented by white, dark gray, and red balls, respectively.

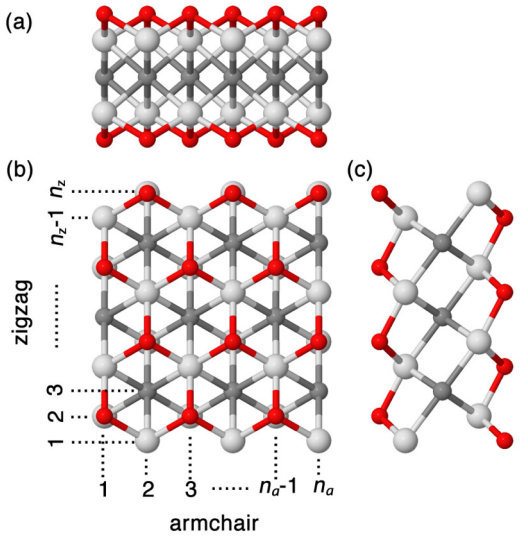

FIG. 2. Schematic of 1D nanoribbon cut from a 2D MXene in model I structure. (a), (c) are side views and (b) is top view of the nanoribbon. In (b), armchair (zigzag) nanoribbon is periodic in the vertical (horizontal) direction. The size parameter n_a (n_z) for armchair (zigzag) is defined according to the number of atomic lines in the vertical (horizontal) direction. M, X, and T elements are represented by white, dark gray, and red balls, respectively.

$Sc_2C(OH)_2$ in armchair and zigzag configurations. Finally, our results are summarized in Sec. IV.

II. COMPUTATIONAL METHODS AND MODELS

First-principles calculations are carried out within the framework of density functional theory (DFT) using the projector augmented wave method as implemented in the Vienna *ab initio* simulation package (VASP) code, and the exchange-correlation functional of Perdew-Burke-Ernzerhof (PBE). Plane-wave energy cutoff is set as 450 eV. The structures are fully optimized with a maximum force criterion of 10^{-2} eV/Å. For 2D MXenes, $12 \times 12 \times 1$ and $42 \times 42 \times 1$ Monkhorst-Pack k-point grids are used during structural optimization and DOS calculations, respectively. For 1D nanoribbons, the corresponding k-point grids are $8 \times 1 \times 1$ and $24 \times 1 \times 1$. The 2D MXene sheets are separated from each other in the nonperiodic direction by a large vacuum of 20 Å. 1D nanoribbons are separated from each other by 20 Å and 10–20 Å (depending on the size of the nanoribbon) in the nonperiodic directions perpendicular to and along the plane of the nanoribbon, respectively. We perform convergence tests for all the parameters mentioned above to ensure the accuracy of the calculations. During our structural optimizations, we do not impose any symmetry, and we perform several calculations for the same structure starting with different initial magnetic moments for the transition-metal element to ensure that the final optimized structures have the lowest energy.

As discussed in previous studies [39,40,55], three types of structural models for 2D M_2XT_2 are considered in this work (shown in Fig. 1). In model I, the top-layer T atoms are directly above the lower-layer M atoms while the bottom-layer T atoms are directly below the upper-layer M atoms (this is the so-called A site for T atoms). In model II, the top-layer (bottom-layer) T atoms are right above (below) the X atoms (this is the B site for T atoms). Model III is a combination of models I and II, in which the top-layer T atoms are right above the lower-layer M atoms (A site), while the bottom-layer T atoms are right below the X atoms (B site). Hydrogen atoms in OH terminations are placed on top of the oxygen atoms.

The 1D MXene nanoribbons are constructed by cutting a strip from the 2D sheet along either of the two (orthogonal) directions which result in armchair or zigzag type nanoribbons. This is shown for a model I type nanoribbon in Fig. 2. The corresponding armchair nanoribbons (ANRs) and zigzag nanoribbons (ZNRs) are characterized by size parameters n_a and n_z, respectively, and denoted as n_a-ANR and n_z-ZNR. For ANRs, one can have only two types of structures: those ANRs with an odd-size parameter n_a have symmetric edges (with respect to a line passing through the middle of the ribbon and parallel to the periodic direction), while those with an even-size parameter are asymmetric. The classification is more complicated for ZNRs due to two different kinds of atomic lines extending along the periodic direction. These atomic lines contain either rows of M/T atoms (with M atoms on top of T atoms or vice versa, which we denote as M for short) or rows of X atoms. The order of the atomic lines in ZNRs can be represented as $\ldots MMXMMX\ldots$, resulting in three types of edges which are MMX, MXM, and XMM, where the first letter denotes the outermost atomic line. Considering all combinations of starting and ending edges, six types of ZNR structures can, therefore, be achieved, as shown in Fig. S1 in the Supplemental Material [56]. (1) n_z-(MMX-MMX)-ZNR, where $n_z = 3p$ (p is a positive integer), representing ZNRs with the size of n_z and two edges of MMX and XMM; (2) n_z-(MXM-MXM)-ZNR, where $n_z = 3p$; (3) n_z-(MMX-MXM)-ZNR, where $n_z = 3p + 1$; (4) n_z-(XMM-MMX)-ZNR, where $n_z = 3p + 1$; (5) n_z-(MMX-XMM)-ZNR, where $n_z = 3p + 2$; and (6) n_z-(MXM-MMX)-ZNR, where $n_z = 3p + 2$.

TABLE I. Optimized lattice constants (a, in Å) along with the corresponding lowest-energy structural models (in parentheses) and band gaps (E_g, in eV) for 2D MXenes (M = Ti, Zr, Hf, Sc, Y, La) with different functional groups (O, F, OH).

	O		F		OH	
MXene	a	E_g	a	E_g	a	E_g
Ti_2C	3.04 (I)	0.32	3.06 (I)		3.08 (I)	
Zr_2C	3.31 (I)	0.97	3.30 (I)		3.31 (I)	
Hf_2C	3.27 (I)	1.03	3.27 (I)		3.28 (I)	
Sc_2C	3.44 (III)	1.86	3.29 (I)	1.03	3.31 (I)	0.56
Y_2C	3.72 (III)	1.32	3.57 (I)	1.14	3.59 (I)	0.47
La_2C	4.00 (III)	0.60	3.87 (I)	1.02	3.89 (I)	0.64

According to these definitions, Fig. 2 shows a 6-ANR or 11-(MMX-XMM)-ZNR (depending on whether the vertical or the horizontal direction is taken as the periodic direction of the nanoribbon). Similarly, model II nanoribbons can be also classified into two types of ANRs and six types of ZNRs, while model III nanoribbons can be classified into two types of ANRs and nine types of ZNRs due to three different kinds of atomic lines that they possess (shown in Fig. S2 in the Supplemental Material [56]). The details of model III ZNRs will be discussed in Sec. III C.

III. RESULTS AND DISCUSSION

A. 2D MXenes

Twelve 2D MXenes, Ti_2CO_2, Zr_2CO_2, Hf_2CO_2, Sc_2CO_2, Sc_2CF_2, $Sc_2C(OH)_2$, Y_2CO_2, Y_2CF_2, $Y_2C(OH)_2$, La_2CO_2, La_2CF_2, $La_2C(OH)_2$, are found to be semiconducting. The optimized lattice constants, ground-state structural models (I, II, or III) and PBE band gaps for these 2D MXenes are listed in Table I. Model II is found to be the least favorable structure among the three models for all systems considered. The ground-state structures of Ti_2CO_2, Zr_2CO_2, Hf_2CO_2, Sc_2CF_2, $Sc_2C(OH)_2$, Y_2CF_2, $Y_2C(OH)_2$, La_2CF_2 and $La_2C(OH)_2$ have the atomic configuration of model I, while Sc_2CO_2, Y_2CO_2, and La_2CO_2 have ground-state structures corresponding to model III. The lowest-energy structure of 2D MXenes is found to be dependent on the oxidation states of transition-metal elements: If the transition metal can provide sufficient electrons for both C and the functional groups, then model I is the energetically preferred configuration; otherwise, model III becomes the lowest-energy structure, in which the functional groups can acquire the necessary electrons by hybridization with C atoms. These findings are consistent with observations in previous studies [39,40].

The calculated band structures of all the semiconducting MXenes are plotted in Fig. 3. Among the 12 semiconducting MXenes, Ti_2CO_2, Zr_2CO_2, Hf_2CO_2, Sc_2CO_2, Sc_2CF_2, $Sc_2C(OH)_2$ have already been reported in the literature with band gaps of 0.24, 0.88, 1.0, 1.8, 1.03, and 0.45 eV, respectively, at the PBE level [39], which are slightly lower than, but still within 0.1 eV of, our results shown in Table I. Ti_2CO_2, Zr_2CO_2, and Hf_2CO_2 with model I ground-state structures have indirect band gaps from Γ to M point of the Brillouin zone, which increase in going from Ti to Hf, while

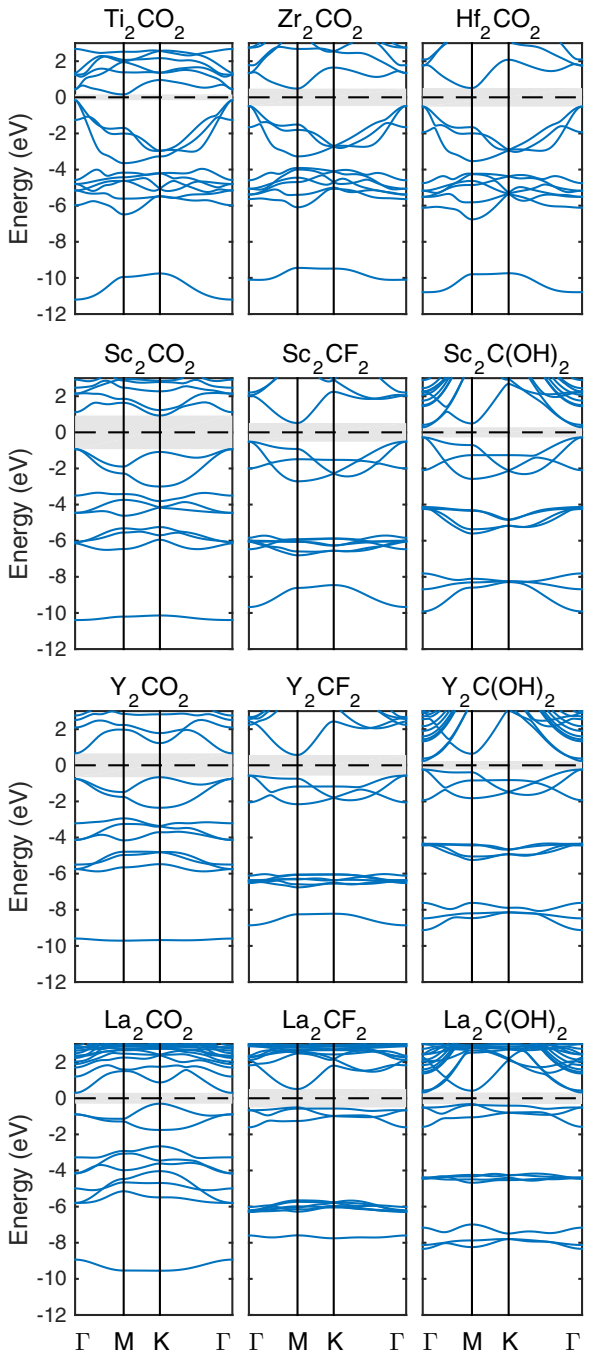

FIG. 3. Band structures of semiconducting 2D MXenes. Fermi energy is shifted to zero and the band gap is highlighted by the shaded area.

Sc_2CO_2, Y_2CO_2, and La_2CO_2 with model III ground-state structures have indirect band gaps from Γ to K point, which decrease in going from Sc to La. This shows that the particular ground-state atomic configuration plays a significant role in the evolution of band gaps in a given group. Compared to those functionalized with F, MXenes with OH groups have extra conduction bands near the Fermi level at the Γ point due to the intrinsic dipole moment in OH [53]. As a result, $Sc_2C(OH)_2$ and $Y_2C(OH)_2$ exhibit direct band gaps at Γ point. Functionalized MXenes with Y or La have not been

reported in previous studies; however, they are all found to be semiconductors with sizable band gaps in our calculations. We note that the quasiparticle gaps including many-body effects are likely to be considerably higher than those reported here for both 2D MXenes and the nanoribbons at the PBE level. Preliminary studies show that the GW band-gap corrections for Ti_2CO_2 can be as high as 1 eV [57].

B. Ti_2CO_2 nanoribbons

Ti-MXenes have become the most intensively studied class of materials among all MXenes, mainly due to the fact that Ti_2C and Ti_3C_2 have been produced in experiments [32]. Among the functionalized Ti-MXenes, Ti_2CO_2 is the only one that has been found to be semiconducting, and here we use it as a prototype to study the size and edge effects in MXene nanoribbons. Since Zr and Hf are in the same group as Ti, we expect Zr- and Hf-based MXene nanoribbons functionalized with O to exhibit similar structural and electronic trends to those presented below [58].

1. Armchair nanoribbons

Ti_2CO_2 ANRs of different widths (controlled by the size parameter n_a) are constructed from the 2D Ti_2CO_2 sheet with n_a ranging from 2 to 20, and are fully relaxed. Our results show that all the Ti_2CO_2 nanoribbons with armchair edges inherit the semiconducting character of 2D Ti_2CO_2, and their band gaps are significantly dependent on the edge symmetry and width of the nanoribbon. The semiconducting character of ANRs has also been found in other 2D systems such as graphene, boron nitride, and TMDs [2,17,22,23].

Figure 4 shows the total density of states (TDOS) and projected density of states (PDOS) for Ti_2CO_2 2D sheet and two representative ANRs, 6-ANR (asymmetric) and 7-ANR (symmetric). The conduction band of the 2D sheet is primarily due to Ti $3d$ states, whereas the valence states between -6 and 0 eV can be divided into two subbands: subband I between ~ -4 and 0 eV, which has almost equal contributions from Ti $3d$, C $2p$, and O $2p$, and subband II between ~ -6 and -4 eV dominated primarily by O $2p$ orbitals with some Ti $3d$ character due to the strong hybridization between them. Subbands I and II are separated by a small gap ($\sim$0.3 eV). As shown in Figs. 4(b) and 4(c), while the size of the band gap is considerably different in the two types of ANRs, it is clear that both of them have gaps at the Fermi level rendering them as semiconductors. In the PDOS of 6-ANR and 7-ANR, subband II shifts upward and merges with subband I. Apart from this small change and the increase in the band gap, the orbital characters of the bands for 6-ANR are very similar to those of the 2D sheet. However, for the 7-ANR there is an extra sharp peak, contributed mainly by Ti $3d$ states with small mixture of O $2p$ states, just above the valence band maximum (VBM), forming the conduction band minimum (CBM) which will be discussed later in this section.

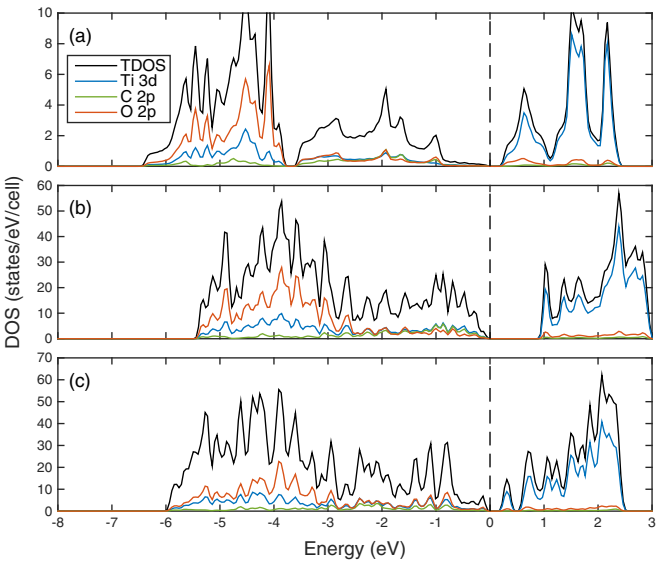

FIG. 4. TDOS and PDOS on selected atomic orbitals of (a) 2D Ti_2CO_2, (b) Ti_2CO_2 6-ANR, and (c) Ti_2CO_2 7-ANR. Fermi energy is shifted to zero at the top of valence bands.

TABLE II. Number of dangling bonds D for different types of edges in the unit cell of Ti_2CO_2 nanoribbons. The subscript Ti-C represents the Ti dangling bond with C removed.

	$D_{\text{Ti-C}}$	$D_{\text{Ti-O}}$	$D_{\text{C-Ti}}$	$D_{\text{O-Ti}}$
ANR edge	2	2	2	2
ZNR-CTiTi edge	0	1	3	1
ZNR-TiTiC edge	3	1	1	0
ZNR-TiCTi edge	1	2	1	2

The semiconducting character of Ti_2CO_2 ANRs can be explained by an electron counting (EC) rule: an ANR of width n_a has a stoichiometric unit cell with a composition of $(Ti_2CO_2)_{n_a}$. In the unit cell of 2D Ti_2CO_2 sheet, each Ti atom (with four valence electrons) can provide two electrons for C to form a Ti-C bond and two electrons for the neighboring O atom to form a Ti-O bond. This results in filling of p orbitals of both C and O, while leaving the Ti d states empty. As shown in Table II, when an ANR is cut from the 2D sheet, each of the two ANR edges ends up with four Ti dangling bonds, two C dangling bonds and two O dangling bonds in the unit cell. Accordingly, the Ti dangling bonds provide the required extra electrons (eight per edge per unit cell) to saturate the dangling bonds of both C and O. Thus, as in the 2D sheet, the valence bands of ANRs originate primarily from the filled p orbitals of C and O atoms, while the conduction bands are formed from the (empty) Ti $3d$ orbitals. We note there is only one type of edge for ANRs. This is clearly evident for symmetric ANRs, while for asymmetric ones, one edge is a uniform shift with respect to the other by half the unit-cell parameter along the periodic direction. Therefore, the EC rule is satisfied for both edges, which makes it possible for all ANRs to restore the semiconducting character of the 2D sheet. As we will see later for the case of ZNRs, when either edge fails to satisfy the electron counting rule, this makes the corresponding nanoribbon have a metallic character.

Next, we discuss the variation of the band gap of ANRs as a function of size, plotted in Fig. 5. It can be seen that the evolution of the band gap for asymmetric (with even n_a) and symmetric ANRs (with odd n_a) as a function of size is

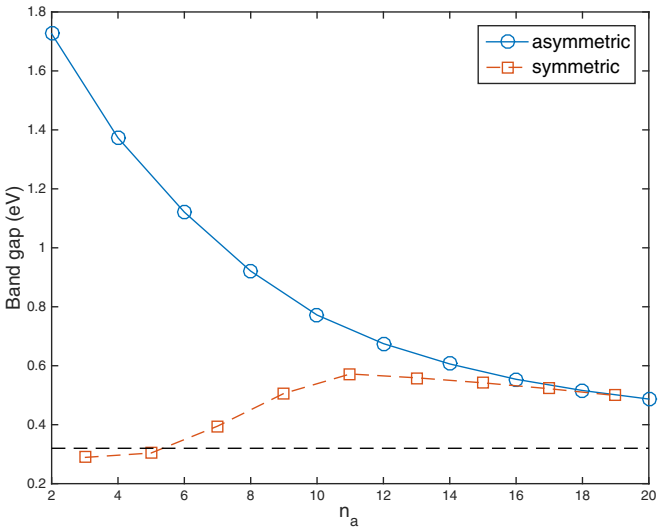

FIG. 5. Band-gap variation as a function of size n_a ($n_a = 2$–20) for Ti_2CO_2 ANRs. The blue curve with circles shows asymmetric ANRs with even n_a, the red curve with squares shows symmetric ANRs with odd n_a. The dashed line marks the band gap of 2D Ti_2CO_2.

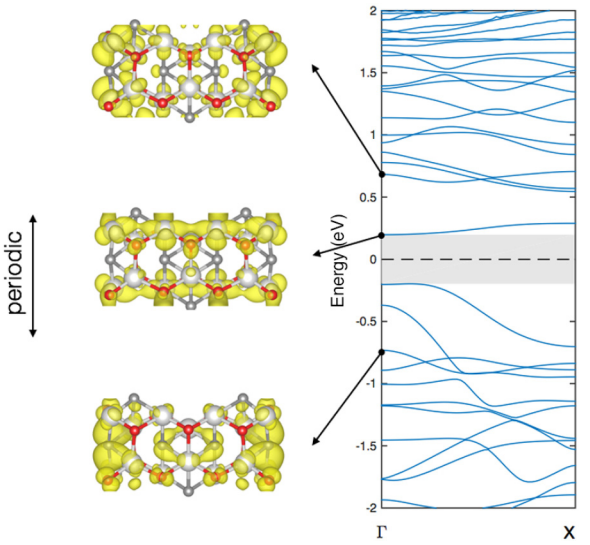

FIG. 6. Top view of charge density isosurfaces (isovalue is set as 0.02 $e^-/Å^3$) for selected points in the band structure of Ti_2CO_2 7-ANR. Ti, C, and O are represented by white, dark gray, and red balls, respectively. The middle isosurface shows the state due to the significant Ti d-d hybridization which is discussed in detail in the text, while the other two isosurfaces show the edge states that appear at higher (lower) energies compared to CBM (VBM). The Fermi energy is shifted to zero at the center of the band gap.

quite different at small sizes. As the width of the nanoribbons increases, this difference disappears, and the band gaps of both types of ANRs slowly converge to the band gap of the 2D Ti_2CO_2 which is 0.32 eV at the PBE level. The band gaps of small-sized asymmetric ANRs increase dramatically as the ribbon size decreases due to quantum confinement [59]. However, for small-sized symmetric ANRs (such as for $n_a = 3$ and 5), the band gaps are even smaller than that of the 2D sheet. This unusual band-gap variation is due to the appearance of a sharp peak in the DOS, mentioned above, arising from a very flat band just above the VBM, as shown in Fig. 6 for the case of 7-ANR. This flat band has predominantly Ti d_{xy} character with a very small O $2p$ admixture, and occurs in small-sized symmetric ANRs ($n_a < 10$). As shown in Fig. 6, this band is associated with a particular row of Ti atoms spanning the width of the ANR. The presence (absence) of this flat band in the band structure of symmetric (asymmetric) ANRs is intimately related to the particular geometry and relaxation patterns of the two different types of ANRs, as we briefly explain below focusing on $n_a = 6$ and 7.

The relaxed structures of the unit cell of 6- and 7-ANR are shown in Fig. 7. Before relaxation, an ANR of width n_a can be viewed as a layered structure with one Ti_2CO_2 in each layer per unit cell and equal spacings between two adjacent layers across the width of the ribbon. Upon relaxation, the two outermost layers are always observed to be tightly bound to each other and have weaker interactions with (farther away from) the third layer from the edge. For small sizes ($n_a \leqslant 10$), the asymmetric ANRs with an even number of layers are observed to form a series of separated bilayers, while the symmetric ANRs with an odd number of layers have a symmetry plane at the center of the ribbon, which prevents the formation of separated bilayers in the middle of the ribbon. As a result of these different relaxation patterns, the Ti-Ti distances across the width of the ribbon are different for the two types of ANRs. As shown in Fig. 7, there are two rows of Ti atoms along the ribbon width in each unit cell. For asymmetric ANRs with an even n_a, there are $n_a/2$ Ti atoms in each row (three atoms in each row for the 6-ANR as shown). For symmetric ANRs with an odd n_a, there are $(n_a + 1)/2$ Ti atoms in one row and $(n_a - 1)/2$ Ti atoms in the other (four atoms in one row and three atoms in the other for the 7-ANR as shown). In the 6-ANR, the average relaxed Ti-Ti distance in each row is 3.03 Å, very close to the corresponding Ti-Ti distance in the 2D sheet, which is 3.04 Å. In the 7-ANR, the average relaxed Ti-Ti distances in the four-atom and three-atom rows are 2.92 and 3.21 Å, respectively. Therefore, the four-atom row is significantly compressed by ∼4% while the three-atom row is stretched by ∼5.6% after relaxation.

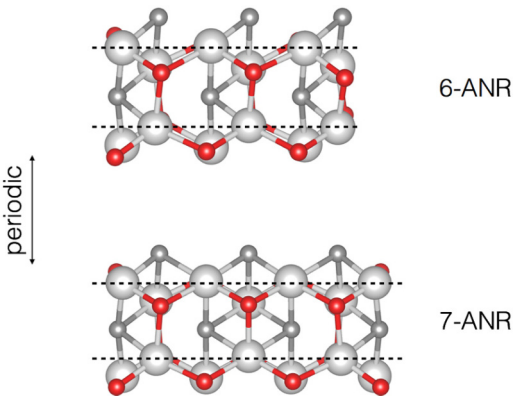

FIG. 7. Top view of the relaxed structures of Ti_2CO_2 6-ANR and 7-ANR unit cells. Ti, C, and O are represented by white, dark gray, and red balls, respectively. The featured Ti rows are marked by black dashed lines.

The flat band of predominantly Ti d_{xy} character mentioned above originates from Ti atoms in this four-atom row due to the significant reduction in the Ti-Ti distance which allows for an appreciable d-d hybridization. In the 6-ANR, there is no such Ti d-d interaction, and the bands near the Fermi level look quite similar to the bands in the 2D sheet, other than a considerable increase in the band-gap value due to quantum confinement. After $n_a = 10$, the central part of the nanoribbon begins to converge to the geometry of the 2D sheet, reducing the tendency to form separated bilayers in asymmetric ANRs and Ti d-d interaction in symmetric ANRs. Therefore, the band gaps of both asymmetric and symmetric ANRs converge (albeit slowly) to the value for the 2D sheet as n_a gets larger and larger. The similar even-odd oscillation behavior of band gaps has also been reported for rutile TiO_2 ultrathin films [60]. Finally, we note that ANRs also have states in the vicinity of the band gap that are mainly localized at the edges, however, these edge states appear higher up (lower down) in the conduction (valence) band manifold, as shown in Fig. 6 for $n_a = 7$.

2. *Zigzag nanoribbons*

Since a ZNR edge is determined by the atomic composition and sequencing of the three outermost atomic lines, we considered ZNRs with n_z larger than 6 in order to study the edge effects on the nanoribbon. Furthermore, ZNRs with $n_z < 9$ are found to undergo significant reconstructions after relaxation since their widths and thicknesses are comparable to each other (they are more like nanorods). Thus, in the following discussion, we focus on sizes from $n_z = 9$ to 23. Since there are two ZNRs with different edge structures for a given n_z, this means we focus on 30 different ZNRs. In other words, in terms of the six different ZNR types introduced in Sec. II, we consider five different sizes for each ZNR type. Distinct from the ANRs, most of the Ti_2CO_2 ZNRs are found to be metallic. Similar observations have been reported for 2D MoS_2 and $NiSe_2$, whose ZNRs without hydrogen passivation are all metals whereas their 2D sheets are semiconductors [22,23].

The spin-resolved TDOS of six types n_z-ZNR ($n_z = 9$–11) are plotted in Fig. 8. Only the 9-(TiCTi-TiCTi)-ZNR is found to be a semiconductor whereas others are all metallic. Among these metallic ZNRs, 9-(TiTiC-TiTiC)-ZNR, 10-(TiTiC-CTiTi)-ZNR, 10-(CTiTi-TiTiC)-ZNR, and 11-(TiCTi-TiTiC)-ZNR have net magnetic moments, while 11-(TiTiC-CTiTi) is nonmagnetic. The electronic and magnetic properties of larger ($n_z > 11$) ZNRs follow the same trends.

Similar to the case discussed earlier for ANRs, the semiconducting/metallic nature of ZNRs can be understood using the EC rule. $n_z = 3p$-(TiCTi-TiCTi)-ZNRs have the stoichiometric unit cells and two TiCTi edges. As shown in Table II, TiCTi edge has three Ti dangling bonds, one C dangling bond, and two O dangling bonds in the unit cell. Hence, all of the dangling bonds on C and O atoms can be filled and those on Ti atoms are left empty in a TiCTi type edge. Since both of the edges are saturated and the unit cell is stoichiometric, (TiCTi-TiCTi)-ZNRs are able to restore the semiconducting character of the 2D sheet after edge reconstruction. For CTiTi and TiTiC edges, on the other hand, the excess electrons donated by the Ti dangling bonds cannot fully saturate the C and O dangling bonds (that is, $D_{\text{Ti-C}} + D_{\text{Ti-O}} \neq D_{\text{C-Ti}} + D_{\text{O-Ti}}$ for these edge types, using the notation in Table II). Since the other five types of ZNRs have at least one edge that is of the CTiTi or TiTiC type (as shown in Fig. S1 [56]), they all turn out to be metallic.

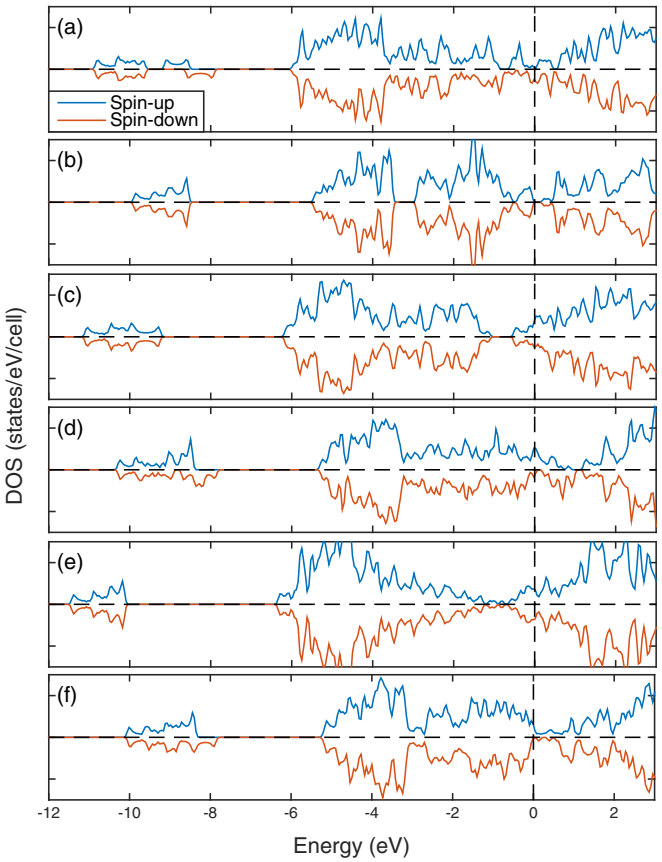

FIG. 8. Spin-resolved TDOS of the six types of ZNRs: (a) 9-(TiTiC-TiTiC)-ZNR, (b) 9-(TiCTi-TiCTi)-ZNR, (c) 10-(TiTiC-TiCTi)-ZNR, (d) 10-(CTiTi-TiTiC)-ZNR, (e) 11-(TiTiC-CTiTi)-ZNR, and (f) 11-(TiCTi-TiTiC)-ZNR. Fermi energy is shifted to zero and set at the top of valence bands for semiconductors.

To provide further support for the explanations above, the PDOS (sum of spin up and down) of the three types of ZNR edges are plotted in Fig. 9. In CTiTi edge, Ti dangling bonds cannot provide enough electrons to saturate the dangling bonds of the outermost C atom (i.e., $D_{\text{Ti-C}} + D_{\text{Ti-O}} < D_{\text{C-Ti}} + D_{\text{O-Ti}}$), thus there is a strong signal of C $2p$ orbital hybridized with Ti $3d$ orbital around Fermi level due to the dangling states in the C atom. In TiTiC edge, there are more Ti dangling bonds than the sum of C and O dangling bonds (i.e., $D_{\text{Ti-C}} + D_{\text{Ti-O}} > D_{\text{C-Ti}} + D_{\text{O-Ti}}$), which leads to Ti atoms not being fully ionized. Hence, the Fermi energy shifts upward and there is a significant contribution to the DOS at the Fermi level due to these Ti $3d$ states, rendering the system metallic. However, in the TiCTi edge, there is a gap between the valence and conduction bands because all the dangling bonds are either saturated or fully empty. Like the 2D Ti_2CO_2, the valence bands of TiCTi edge can also be divided into two subbands I (−3 to 0 eV) and II (−6 to −3 eV) with a gap in the middle. Subband I shows strong hybridization of Ti $3d$–C $2p$ and Ti $3d$–O $2p$ orbitals corresponding to

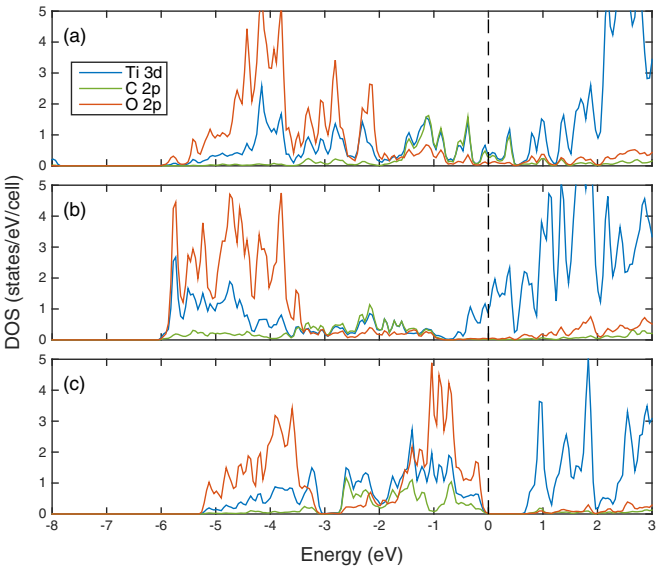

FIG. 9. PDOS (sum of spin up and down) on selected atomic orbitals of (a) CTiTi edge, (b) TiTiC edge, and (c) TiCTi edge for Ti_2CO_2 ZNRs. Two Ti, one C, and one O atoms are considered for each edge. Fermi energy is shifted to zero and set at the top of valence bands for semiconductors.

the Ti-C and Ti-O bonds. Therefore, the TiCTi edge retains the main characteristics of the 2D sheet in this type of nanoribbon. We note that a gap at the Fermi level in the PDOS of a TiCTi edge is present, even though the corresponding ZNR may have metallic character overall. For example, for 10-(TiCTi-CTiTi)-ZNR and 11-(CTiTi-TiCTi)-ZNR, both of which have metallic character overall (since at least one of the edges is not of the TiCTi type), when the PDOS is calculated by projecting onto atomic orbitals centered on atoms at the TiCTi edge, one can observe the opening of the gap at the Fermi level, as shown in Fig. 9(c).

The band gaps of the (TiCTi-TiCTi)-ZNR family are measured to study the size effect on semiconducting ZNRs, as shown in Fig. 10. We find that the band gaps for $n_z \geqslant 12$ decrease and slowly converge to that of 2D sheet (0.32 eV). This band-gap evolution pattern is similar to that of ANRs and can be rationalized by quantum confinement effect. A small exception to this trend occurs for 9-(TiCTi-TiCTi)-ZNR, which has a small band gap of 0.32 eV due to a particularly dispersive conduction band. Our analysis of the wave-function characters for the valence and conduction bands near the band gap shows that edge states typically appear at the CBM [the 9-(TiCTi-TiCTi)-ZNR is an exception to this], but the VBM is bulklike, with filled edge states appearing further down valence band.

C. Sc_2CO_2 nanoribbons

The lowest-energy structure of Sc_2CO_2 2D sheet corresponds to model III in which the two surfaces (below and above the central C layer) are inequivalent since the functional groups are located at different sites (A site and B site). Its nanoribbons can, therefore, be expected to exhibit different structural and electronic properties compared to those of Ti_2CO_2. Since Y and La are in the same group as Sc, we expect Y- and La-based MXene nanoribbons functionalized with O to exhibit similar structural and electronic trends to those presented in the following.

1. Armchair nanoribbons

Sc_2CO_2 ANRs with $n_a = 2$–$10, 20$ are constructed from the 2D sheet and fully relaxed. The relaxed structures for Sc_2CO_2 2D sheet and ANRs at selected sizes ($n_a = 5, 10, 20$) are plotted in Fig. 11. Unlike the symmetric location of the C layer with respect to the two surfaces in model I structures, the C layer in model III structures is closer to the B-site O layer than to the A-site O layer, resulting in a larger atomic concentration at the lower surface of the sheet as shown in Fig. 11. When a nanoribbon is cut from the 2D sheet, since

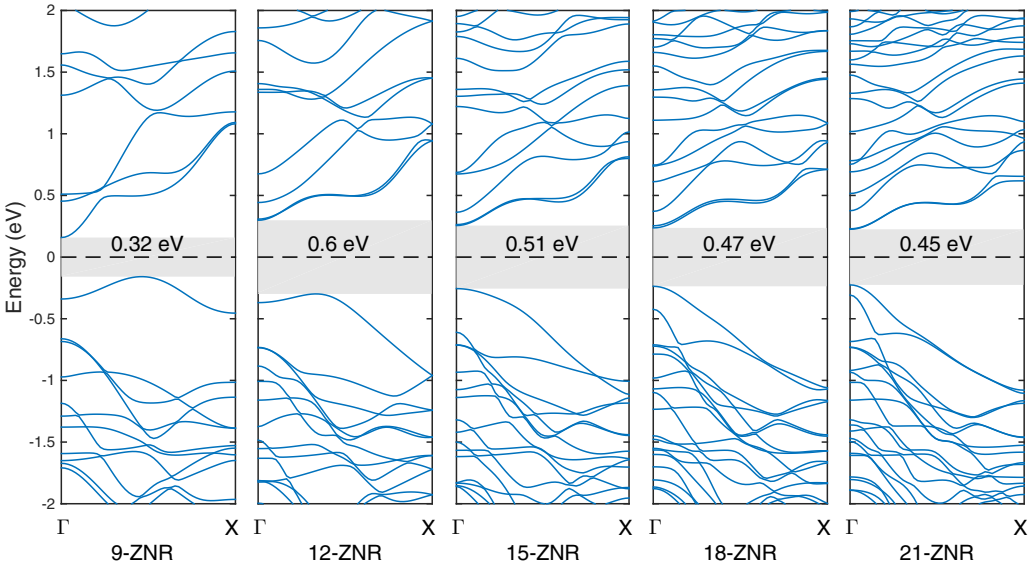

FIG. 10. Band structures of semiconducting Ti_2CO_2 ZNRs ($n_z = 9$–21). Fermi energy is shifted to zero and set at the center of the band gap.

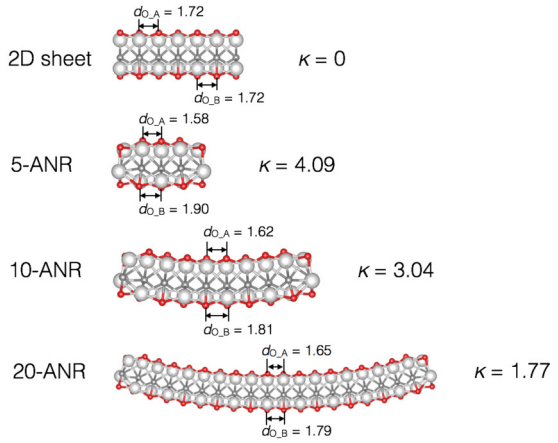

FIG. 11. Side view of the relaxed structures of the 2D sheet, 5-ANR, 10-ANR, and 20-ANR unit cells for Sc_2CO_2. The averaged distance for A-site (B-site) O atoms d_{O_A} (d_{O_B}) in Å is labeled for each structure, along with the curvature κ in units of 10^{-2}/Å. Sc, C, and O are represented by white, dark gray, and red balls, respectively.

periodicity is no longer imposed across the ribbon width, this atomic concentration imbalance at the two surfaces can be relieved by stretching and compressing of the two surfaces. As a result, the lowest-energy structures of model III nanoribbons are not flat, but rather bent as shown with some examples in Fig. 11. We can quantify this bending by computing the curvature $\kappa = 1/R$, where R is the radius of the circle fitted to the positions of the the B-site O groups (the lower layer of O atoms shown in the insets). As we can see from Fig. 11, κ decreases as the n_a increases, which means the curvature effect gets weaker as the nanoribbon grows, as expected. The curvature of MXene has already been observed in experiments [32], where some functionalized Ti_3C_2 nanosheets are bent to radius less than 20 nm (i.e., $\kappa \geqslant 0.5 \times 10^{-2}$/Å).

Similar to Ti_2CO_2 ANRs, Sc_2CO_2 ANRs are found to be semiconducting, which can also be explained by EC rule. However, the bonding mechanism in Sc_2CO_2 2D sheet is different from that in Ti_2CO_2 2D sheet due to their different structural models. In the unit cell of Sc_2CO_2 2D sheet, A-site Sc (with three valence electrons) can provide two electrons for A-site O and one electron for C, while B-site Sc can provide two electrons for C and one electron for B-site O. As a result, both C and the B-site O have one of their $2p$ orbitals containing only one electron. These two orbitals hybridize with each other and can form C-O bonding and antibonding states [39]. The C-O bonds are shown in Fig. 11. An ANR of width n_a has a stoichiometric unit cell with a composition of $(Sc_2CO_2)_{n_a}$. When an ANR is cut from the 2D sheet, the C-O bond is not broken and each of the two ANR edges ends up with four Sc dangling bonds, two C dangling bonds and two O dangling bonds in the unit cell as shown in Table III. Accordingly, the Sc dangling bonds can provide the required extra electrons (six per edge per unit cell) to saturate the dangling bonds of both C and O, restoring the system as semiconductor. It is noteworthy that due to the curvature of nanoribbon, the edge A-site Sc and B-site O atoms form a new Sc-O bond as shown in Fig. 11. Therefore, the edge A-site Sc provides one electron to A-site O and two electron to C, while the B-site Sc provides each of the A-site O, B-site O, and C with one electron, which results in the edge reconstruction. This can be seen in the PDOS of ANR edge shown in Fig. 12(b), where a strong signal of Sc $3d$–O $2p$ hybridization appears at around −0.5 eV.

TABLE III. Number of dangling bonds D for different types of edges in the unit cell of Sc_2CO_2 nanoribbons. The subscript Sc-C represents the Sc dangling bond with C removed.

	$D_{Sc\text{-}C}$	$D_{Sc\text{-}O}$	$D_{C\text{-}Sc}$	$D_{O\text{-}Sc}$
ANR edge	2	2	2	2
ZNR-CScO edge	0	1	3	2
ZNR-OScC edge	3	2	0	1
ZNR-OCSc edge	1	1	2	1
ZNR-ScCO edge	1	2	1	1
ZNR-COSc edge	0	0	3	2
ZNR-ScOC edge	3	2	0	0

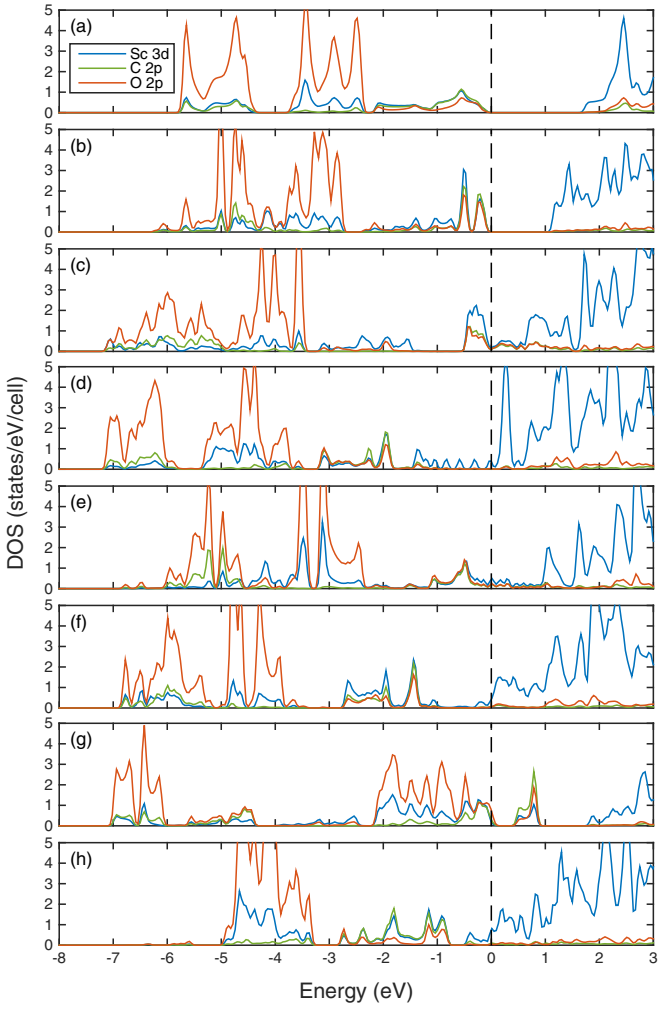

FIG. 12. PDOS on selected atomic orbitals of (a) 2D Sc_2CO_2, (b) ANR edge, (c) ZNR-CScO edge, (d) ZNR-OScC edge and (e) ZNR-OCSc edge, (f) ZNR-ScCO edge, (g) ZNR-COSc edge, (h) ZNR-ScOC edge. Two Sc, one C, and one O atoms are considered for each edge. Fermi energy is shifted to zero and set at the top of valence bands for semiconductors.

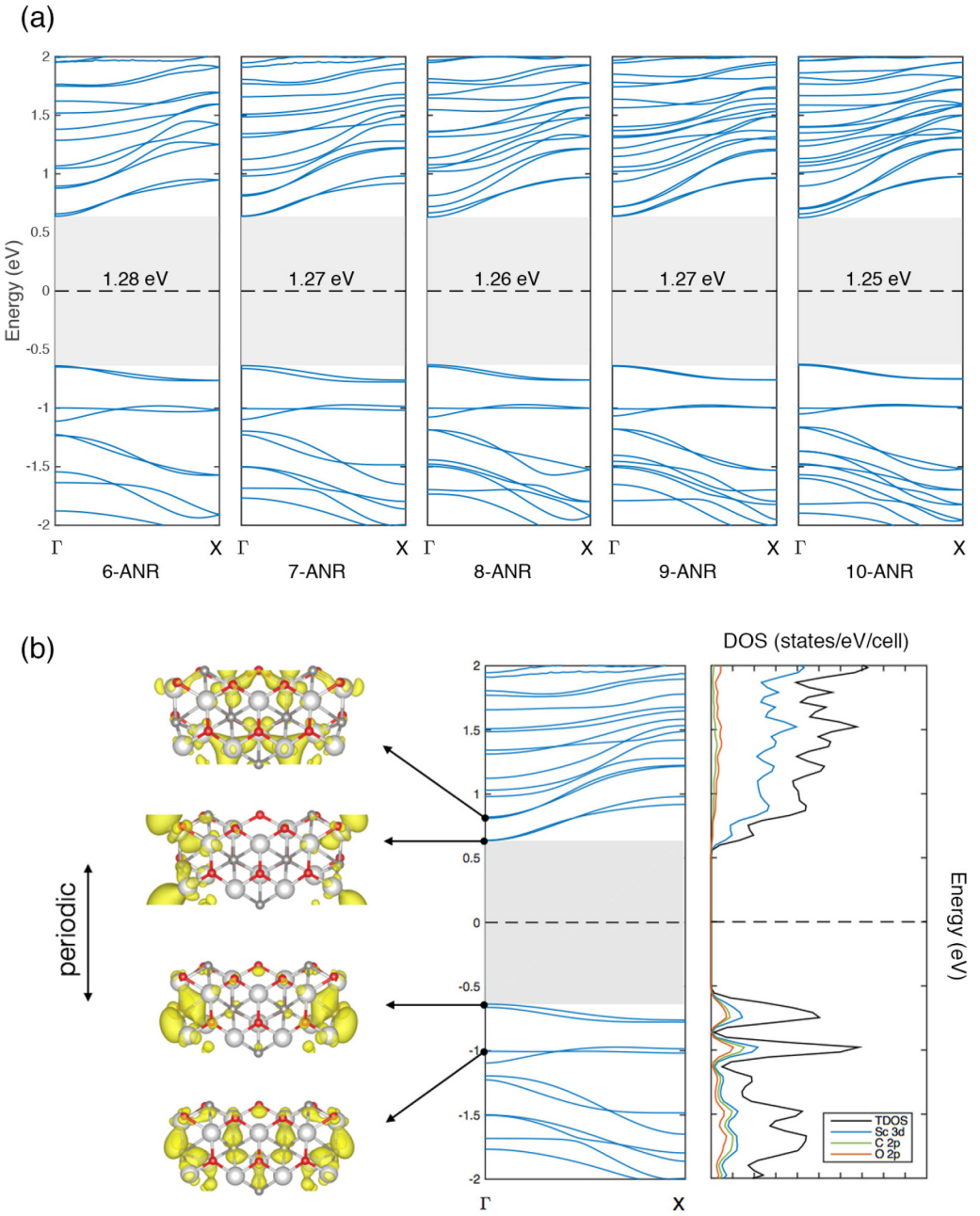

FIG. 13. (a) Band structures of Sc_2CO_2 ANRs ($n_a = 6$–10). Fermi energy is shifted to zero and band gaps are highlighted by the shaded area with corresponding values. (b) Left panel: charge density isosurface (isovalue is set as 0.02 $e^-/\text{Å}^3$) for selected points in the band structure of Sc_2CO_2 7-ANR; right panel: the corresponding TDOS and PDOS on specific atomic orbitals.

The band-structure evolution for Sc_2CO_2 ANRs ($n_a = 6$–10) is plotted in Fig. 13(a). Distinct from Ti_2CO_2, the band gaps of Sc_2CO_2 ANRs are nearly size independent with band-gap values around 1.27 eV, which is lower than that of the 2D sheet (1.86 eV). The reduction in the band gap compared to the 2D sheet is due to appearance of strong edge states that now form the VBM and CBM as shown in Fig. 13(b). This is unlike what is observed in the Ti_2CO_2 ANRs, where the edge states also appear in the band structure, but they are further up (down) in the conduction (valence) bands as shown in Fig. 6. The edge states in Sc_2CO_2 ANRs can be attributed to the edge reconstruction as discussed before. Without these edge states, the band gaps would increase to values that are comparable to that of the 2D sheet. These results indicate the importance of the underlying structural model in determining the band gap of the ANRs.

2. *Zigzag nanoribbons*

As mentioned earlier in Sec. II, model III ZNRs have more complicated edge structures. As shown in Fig. S2 [56], the sequence of the atomic lines in Sc_2CO_2 ZNRs is . . . O/Sc-Sc-C/O-O/Sc-Sc-C/O . . ., resulting in six types of edges which are O/Sc-Sc-C/O, C/O-Sc-O/Sc, Sc-C/O-O/Sc, O/Sc-C/O-Sc, C/O-O/Sc-Sc, and Sc-O/Sc-C/O. Considering all combinations of starting and ending edges, nine types of ZNRs can, therefore, be achieved. Here, we use O, C, and Sc to represent

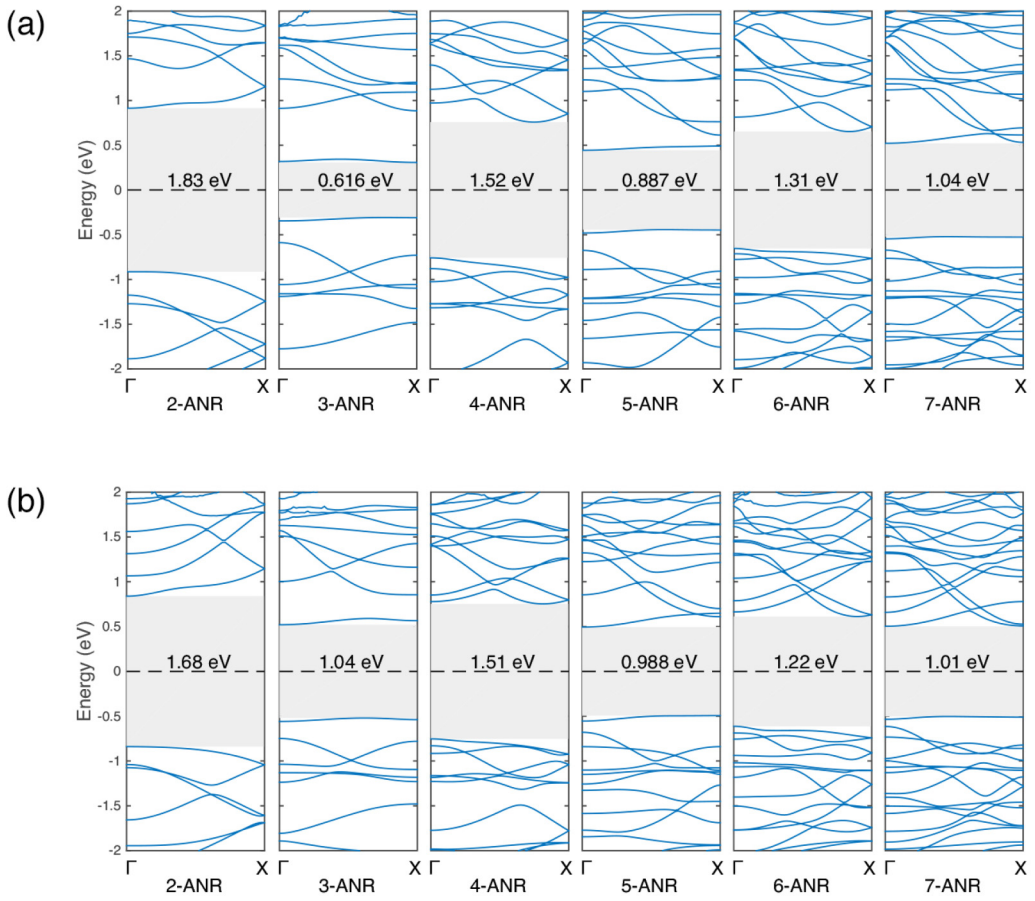

FIG. 14. Band structures of (a) Sc_2CF_2 ANRs and (b) $Sc_2C(OH)_2$ ANRs ($n_a = 2$–7). Fermi energy is shifted to zero and band gaps are highlighted by the shaded area with corresponding values.

O/Sc, C/O, and Sc lines, respectively. For instance, 9-(OScC-OScC)-ZNR represents ZNR with nine atomic lines and two edges of O/Sc-Sc-C/O and C/O-Sc-O/Sc. The nine types of ZNRs with $n_z = 9$–11 are constructed and fully relaxed.

All types of model III ZNRs are observed to be metallic. Again, the metallic nature of these ZNRs can be understood using the EC rule, which is similar to the case discussed for Ti_2CO_2 ZNRs. As shown in Table III, for each ZNR edge type, $D_{\text{Sc-C}} + D_{\text{Sc-O}} \neq D_{\text{C–Sc}} + D_{\text{O-Sc}}$. Therefore, none of the six types of ZNR edges can be saturated, rendering the ZNRs as metals.

The PDOS of the six types of ZNR edges are plotted in Figs. 12(c)–12(h) to provide support for the EC rule explained above. In OScC, ScCO, and ScOC edges, there are more Sc dangling bonds than the sum of C and O dangling bonds (i.e., $D_{\text{Sc-C}} + D_{\text{Sc-O}} > D_{\text{C-Sc}} + D_{\text{O-Sc}}$), which leads to Sc atoms not being fully ionized. Thus, the Fermi energy shifts upward compared to that in the 2D sheet, and there is a significant contribution to the DOS at the Fermi level due to these Sc $3d$ states as shown in Figs. 12(d), 12(f), and 12(h). In CScO, OCSc, and COSc edges, Sc dangling bonds cannot provide enough electrons to saturate the dangling bonds of the outermost C and O atoms (i.e., $D_{\text{Sc-C}} + D_{\text{Sc-O}} < D_{\text{C-Sc}} + D_{\text{O-Sc}}$). As shown in Figs. 12(c), 12(e), and 12(g), there are strong signals of C $2p$–Sc $3d$ and O $2p$–Sc $3d$ hybridization around Fermi level due to the dangling states in the C and O atoms.

D. Sc_2CF_2 and $Sc_2C(OH)_2$ nanoribbons

The lowest-energy structure of Sc_2CF_2 and $Sc_2C(OH)_2$ 2D sheets correspond to model I, thus, the structural and electronic properties of their nanoribbons are expected to have the same trends as Ti_2CO_2 nanoribbons. The two types of ANRs ($n_a = 2$–7) and six types of ZNRs ($n_z = 9$–11) for Sc_2CF_2 and $Sc_2C(OH)_2$ are constructed from their 2D sheets and fully relaxed. All the ANRs are found to be semiconductors. For ZNRs, only the 9-(ScCSc-ScCSc)-ZNR is a semiconductor whereas others are all metals. These results are consistent with Ti_2CO_2 nanoribbons due to the same numbers of dangling bonds at the edges, where the semiconducting/metallic characters can be explained by the EC rule. The results also suggest the significant importance of structural models in determining the electronic properties of the MXene nanoribbons.

The band-gap evolution of both Sc_2CF_2 and $Sc_2C(OH)_2$ ANRs exhibits significant even-odd oscillation as shown in Fig. 14. Sc_2CF_2 has small-sized symmetric ANRs with band gap smaller than that of the 2D sheet (1.03 eV) due to the appearance of Sc d-d hybridization at CBM, which has been discussed in the case of Ti_2CO_2 ANRs. The band gaps of $Sc_2C(OH)_2$ are observed to be larger than that of the 2D sheet (0.56 eV). As we mentioned in Sec. III A, compared to the F-functionalized MXenes, OH-functionalized MXenes have extra conduction bands near the Fermi level at the Γ point due to the intrinsic dipole moment of OH, which reduces

the band gap. When $Sc_2C(OH)_2$ nanoribbons are relaxed, the lack of periodicity across the width of the ribbons and the resulting edge reconstructions lead to significant changes in the directions of the edge OH dipoles as shown in Fig. S4 in the Supplemental Material [56]. Effectively, the net local dipole moment on each surface is then reduced, which increases the band gap of the nanoribbon compared to that of the 2D sheet.

IV. SUMMARY

We studied the size- and edge-dependent properties of MXene nanoribbons using first-principles calculations. The thinnest functionalized MXenes M_2XT_2 with M = Sc, Y, La, Ti, Zr, Hf, X = C, and T = O, F, OH are comprehensively considered in the 2D sheet with three structural models. Twelve of them are found to be semiconducting with band gaps ranging from 0.32 to 1.86 eV at the PBE level. Armchair and zigzag edge-shaped nanoribbons are constructed from the semiconducting MXenes without hydrogen passivation at the edges. These nanoribbons are classified into three and studied with prototypes of (1) Ti_2CO_2, (2) Sc_2CO_2, (3) Sc_2CF_2 and $Sc_2C(OH)_2$. All the ANRs are found to be semiconductors while most of the ZNRs are metals. The semiconducting/metallic nature of the nanoribbons is explained by an electron counting rule, where if all the dangling bonds in both edges can be saturated, then the system remains semiconducting as its 2D counterpart; otherwise, the system becomes metallic due to extra states generated at Fermi level. The lowest-energy structural model plays an important role in determining the structural and electronic properties of the nanoribbons. In nanoribbons corresponding to model I structure (Ti_2CO_2, Sc_2CF_2, and $Sc_2C(OH)_2$), two types of ANRs and six types of ZNRs are defined according to their edge types. The band-gap evolution as a function of the ribbon size of the ANRs exhibits significant even-odd oscillations at small sizes, but the gaps converge to that of the 2D sheet at large sizes. One of the six types of ZNRs which has two semiconducting edges remains as a semiconductor, while the other five types which have at least one metallic edge are metals. Appreciable transition-metal d-d hybridization is observed in some model I nanoribbons, which reduces the band gap by generating a flat band right above the VBM. The band gaps of model I nanoribbons with OH functional groups are found to be considerably larger than those of their 2D counterparts, which is attributed to the significant change in the direction of the OH dipoles at the edges. In nanoribbons corresponding to model III structure with two different surfaces (e.g., Sc_2CO_2), two types of ANRs and nine types of ZNRs are defined. The relaxed ANRs bend after relaxation to relieve the atomic concentration imbalance at the two surfaces, and the curvature decreases as ribbon size grows. The band gaps of model III ANRs are nearly size independent with values that are smaller than that of the 2D sheet, regardless of the ribbon size. The reduction in the band gap compared to the 2D sheet is due to appearance of strong edge states that form the new VBM and CBM. All of the nine types of ZNRs are metallic since none of the ZNR edges is semiconducting as predicted (and verified) by the electron counting rule. Our results suggest that semiconducting versus metallic nature as well as the size of the band gap for semiconducting MXene nanoribbons can be tuned as a function of size, chemical composition, and functional groups, which can be useful for future designs of MXene nanostructures with interesting electronic and optical properties.

ACKNOWLEDGMENTS

This work was supported by the National Science Foundation (Grant No. DMR-1408427) and used resources of the National Energy Research Scientific Computing Center, a DOE Office of Science User Facility supported by the Office of Science of the U. S. Department of Energy under Contract No. DE-AC02-05CH11231.

[1] Y. Xia, P. Yang, Y. Sun, Y. Wu, B. Mayers, B. Gates, Y. Yin, F. Kim, and H. Yan, Adv. Mater. **15**, 353 (2003).
[2] Y.-W. Son, M. L. Cohen, and S. G. Louie, Phys. Rev. Lett. **97**, 216803 (2006).
[3] K. Nakada, M. Fujita, G. Dresselhaus, and M. S. Dresselhaus, Phys. Rev. B **54**, 17954 (1996).
[4] M. Fujita, K. Wakabayashi, K. Nakada, and K. Kusakabe, J. Phys. Soc. Jpn. **65**, 1920 (1996).
[5] K. Wakabayashi, M. Fujita, H. Ajiki, and M. Sigrist, Phys. Rev. B **59**, 8271 (1999).
[6] L. Yang, C.-H. Park, Y.-W. Son, M. L. Cohen, and S. G. Louie, Phys. Rev. Lett. **99**, 186801 (2007).
[7] M. Y. Han, B. Özyilmaz, Y. Zhang, and P. Kim, Phys. Rev. Lett. **98**, 206805 (2007).
[8] V. Barone, O. Hod, and G. E. Scuseria, Nano Lett. **6**, 2748 (2006).
[9] M. Ezawa, Phys. Rev. B **73**, 045432 (2006).
[10] N. Mohanty, D. Moore, Z. Xu, T. Sreeprasad, A. Nagaraja, A. A. Rodriguez, and V. Berry, Nat. Commun. **3**, 844 (2012).
[11] J. Cai, C. A. Pignedoli, L. Talirz, P. Ruffieux, H. Söde, L. Liang, V. Meunier, R. Berger, R. Li, X. Feng *et al.*, Nat. Nanotechnol. **9**, 896 (2014).
[12] Y.-L. Song, Y. Zhang, J.-M. Zhang, and D.-B. Lu, Appl. Surf. Sci. **256**, 6313 (2010).
[13] P. De Padova, O. Kubo, B. Olivieri, C. Quaresima, T. Nakayama, M. Aono, and G. Le Lay, Nano Lett. **12**, 5500 (2012).
[14] L. Pan, H. Liu, X. Tan, H. Lv, J. Shi, X. Tang, and G. Zheng, Phys. Chem. Chem. Phys. **14**, 13588 (2012).
[15] T. H. Osborn and A. A. Farajian, Nano Res. **7**, 945 (2014).
[16] A. Lopez-Bezanilla, J. Huang, H. Terrones, and B. G. Sumpter, Nano Lett. **11**, 3267 (2011).
[17] C.-H. Park and S. G. Louie, Nano Lett. **8**, 2200 (2008).
[18] F. Zheng, G. Zhou, Z. Liu, J. Wu, W. Duan, B.-L. Gu, and S. B. Zhang, Phys. Rev. B **78**, 205415 (2008).
[19] L. Kou, C. Tang, Y. Zhang, T. Heine, C. Chen, and T. Frauenheim, J. Phys. Chem. Lett. **3**, 2934 (2012).
[20] Z. Liu, K. Suenaga, Z. Wang, Z. Shi, E. Okunishi, and S. Iijima, Nat. Commun. **2**, 213 (2011).

[21] K. Dolui, C. D. Pemmaraju, and S. Sanvito, ACS Nano **6**, 4823 (2012).

[22] Y. Li, Z. Zhou, S. Zhang, and Z. Chen, J. Am. Chem. Soc. **130**, 16739 (2008).

[23] J. Reyes-Retana, G. Naumis, and F. Cervantes-Sodi, J. Phys. Chem. C **118**, 3295 (2014).

[24] L. Tapasztó, G. Dobrik, P. Lambin, and L. P. Biró, Nat. Nanotechnol. **3**, 397 (2008).

[25] L. Jiao, L. Zhang, X. Wang, G. Diankov, and H. Dai, Nature (London) **458**, 877 (2009).

[26] J. Cai, P. Ruffieux, R. Jaafar, M. Bieri, T. Braun, S. Blankenburg, M. Muoth, A. P. Seitsonen, M. Saleh, X. Feng *et al.*, Nature (London) **466**, 470 (2010).

[27] X. Wang and Y. Zhou, J. Mater. Sci. Technol. **26**, 385 (2010).

[28] Z. Sun, Int. Mater. Rev. **56**, 143 (2011).

[29] M. W. Barsoum and M. Radovic, Annu. Rev. Mater. Res. **41**, 195 (2011).

[30] M. Naguib, V. N. Mochalin, M. W. Barsoum, and Y. Gogotsi, Adv. Mater. **26**, 992 (2014).

[31] P. Eklund, M. Beckers, U. Jansson, H. Högberg, and L. Hultman, Thin Solid Films **518**, 1851 (2010).

[32] M. Naguib, M. Kurtoglu, V. Presser, J. Lu, J. Niu, M. Heon, L. Hultman, Y. Gogotsi, and M. W. Barsoum, Adv. Mater. **23**, 4248 (2011).

[33] M. Naguib, O. Mashtalir, J. Carle, V. Presser, J. Lu, L. Hultman, Y. Gogotsi, and M. W. Barsoum, ACS Nano **6**, 1322 (2012).

[34] M. Ghidiu, M. R. Lukatskaya, M.-Q. Zhao, Y. Gogotsi, and M. W. Barsoum, Nature (London) **516**, 78 (2014).

[35] M. W. Barsoum, Prog. Solid State Chem. **28**, 201 (2000).

[36] D. Music, Z. Sun, R. Ahuja, and J. M. Schneider, Phys. Rev. B **73**, 134117 (2006).

[37] Z. Sun, D. Music, R. Ahuja, S. Li, and J. M. Schneider, Phys. Rev. B **70**, 092102 (2004).

[38] J. Emmerlich, D. Music, A. Houben, R. Dronskowski, and J. M. Schneider, Phys. Rev. B **76**, 224111 (2007).

[39] M. Khazaei, M. Arai, T. Sasaki, C.-Y. Chung, N. S. Venkataramanan, M. Estili, Y. Sakka, and Y. Kawazoe, Adv. Funct. Mater. **23**, 2185 (2013).

[40] Y. Xie and P. R. C. Kent, Phys. Rev. B **87**, 235441 (2013).

[41] Q. Hu, H. Wang, Q. Wu, X. Ye, A. Zhou, D. Sun, L. Wang, B. Liu, and J. He, Int. J. Hydrogen Energy **39**, 10606 (2014).

[42] Y. Lee, S. B. Cho, and Y.-C. Chung, ACS Appl. Mater. Inter. **6**, 14724 (2014).

[43] S. Zhao, W. Kang, and J. Xue, Appl. Phys. Lett. **104**, 133106 (2014).

[44] S. Wang, J.-X. Li, Y.-L. Du, and C. Cui, Comput. Mater. Sci. **83**, 290 (2014).

[45] Y. Lee, Y. Hwang, S. B. Cho, and Y.-C. Chung, Phys. Chem. Chem. Phys. **16**, 26273 (2014).

[46] B. Anasori, Y. Xie, M. Beidaghi, J. Lu, B. C. Hosler, L. Hultman, P. R. C. Kent, Y. Gogotsi, and M. W. Barsoum, ACS Nano **9**, 9507 (2015).

[47] X.-F. Yu, J.-B. Cheng, Z.-B. Liu, Q.-Z. Li, W.-Z. Li, X. Yang, and B. Xiao, RSC Adv. **5**, 30438 (2015).

[48] S. Zhao, W. Kang, and J. Xue, J. Mater. Chem. C **3**, 879 (2015).

[49] Y. Lee, Y. Hwang, and Y.-C. Chung, ACS Appl. Mater. Interfaces **7**, 7163 (2015).

[50] Z. Guo, J. Zhou, C. Si, and Z. Sun, Phys. Chem. Chem. Phys. **17**, 15348 (2015).

[51] X. Zhang, Z. Ma, X. Zhao, Q. Tang, and Z. Zhou, J. Mater. Chem. A **3**, 4960 (2015).

[52] X. Li, Y. Dai, Y. Ma, Q. Liu, and B. Huang, Nanotechnology **26**, 135703 (2015).

[53] M. Khazaei, M. Arai, T. Sasaki, A. Ranjbar, Y. Liang, and S. Yunoki, Phys. Rev. B **92**, 075411 (2015).

[54] X. Zhang, X. Zhao, D. Wu, Y. Jing, and Z. Zhou, Nanoscale **7**, 16020 (2015).

[55] Q. Tang, Z. Zhou, and P. Shen, J. Am. Chem. Soc. **134**, 16909 (2012).

[56] See Supplemental Material at http://link.aps.org/supplemental/10.1103/PhysRevB.93.115412 for a brief description of four figures related to the structural properties, such as edge terminations of Model I and III zigzag nanoribbons and the relaxed structure of $Sc_2C(OH)_2$, as well as phonon dispersion curves for selected nanoribbons.

[57] Z. Li, L. Hong, F. Jornada, T. Cao, S. Öğüt, and S. G. Louie, APS March Meeting Abstracts, Bulletin of American Physical Society (2015), http://meetings.aps.org/link/BAPS.2015.MAR.T2.7.

[58] In order to check their structural stability, we have computed phonon frequencies for some of the nanoribbons considered (shown in Fig. S3 in the Supplemental Material [56]). No unstable phonon modes have been found, which suggests the structural stability of the proposed structures

[59] H. Haug and S. Koch, *Quantum Theory of the Optical and Electronic Properties of Semiconductors* (World Scientific, Singapore, 1994).

[60] T. Bredow, L. Giordano, F. Cinquini, and G. Pacchioni, Phys. Rev. B **70**, 035419 (2004).